



1 **The miscellaneous synoptic forcings in the four-day widespread extreme rainfall**
2 **event over North China in July 2023**

3
4 Jinfang YIN^{1,2,3}, Feng LI¹, Mingxin LI¹, Rudi XIA¹, Xinghua BAO¹,
5 Jisong SUN¹, and Xudong LIANG¹

6
7 ¹ State Key Laboratory of Severe Weather, Chinese Academy of Meteorological
8 Sciences, Beijing 100081, China

9 ² Research Center for Disastrous Weather over Hengduan Mountains & Low-Latitude
10 Plateau, China Meteorological Administration (CMA), Kunming 650034, China

11 ³ Shigatse National Climatological Observatory, CMA, Shigatse 857000, China

12
13 Submitted to *Natural Hazards and Earth System Sciences (NHESS)*

14 August 2024

15
16 Corresponding author: Jinfang YIN

17 E-mail: yinjf@cma.gov.cn



18

ABSTRACT

19 Synoptic forcings have traditionally played a pivotal role in extreme rainfall over North
20 China. However, there are still large unexplained gaps in understanding the formation of
21 extreme rainfalls over this region. The heavy rainfall event, lasting from 29 July to 2 August
22 2023 (referred to as “23·7” event), is characterized by long duration, widespread coverage,
23 and high accumulated rainfall over North China. Overall, the persistent extreme rainfall is
24 closely associated with the remnant vortex originating from typhoon Doksuri(2305), tropical
25 storm Khanun(2306), and the unusual westward extended western Pacific subtropical high
26 (WPSH), as well as quasi-stationary cold dry air masses surrounding North China on the west
27 and north sides. Based on wind profiles and rainfall characteristics, the life history of the
28 “23·7” event is divided into two stages. In the first stage, the western boundary of the western
29 Pacific subtropical high (WPSH) was destroyed by the tropical storm Doksuri, appearing that
30 the WPSH retreated eastward with decreasing height. As a result, an inclined vertical
31 distribution on the western boundary was established below 500 hPa. Therefore, convections
32 were limited by the tilted WPSH with warm-dry cover embedded in the low-to-middle
33 troposphere. Meanwhile, the orography in the west of North China was controlled by cold air
34 masses above nearly 3.0 km. Combining the orographic and cold air blockings, only a shallow
35 southeasterly layer (between 1.3 and 3.0 km) can overpass mountains. Although the warm
36 and moist southeasterly flows were lifted by orography, no convections were triggered
37 because of the local capped cold and dry air masses overhead. Under this framework,
38 equivalent potential temperature (θ_e) gradients were established between warm humid and
39 dry cold air masses, similar to a warm front, causing warm air to lift and generate widespread
40 rainfall but low intensity. However, the lifting was too weak to allow convection to be highly
41 organized. In the second stage, the WPSH was further destroyed by enhanced Khanun, and
42 thus the embedded warm-dry cover associated with the tilted WPSH was significantly thinned.
43 Consequently, convections triggered by orographic blocking can move upward and
44 consequently further develop, forming deep convections. Comparatively speaking, the
45 convections in the second stage are much deeper than those in the first stage. The results
46 gained herein may shed new light on better understanding and forecasting of long-lasting
47 extreme rainfall.



48 **1. Introduction**

49 A persistent severe rainfall event occurred over central and North China during the period
50 from 29 July to 2 August 2023, which was regarded as one of the precipitation extremes of 2023
51 globally (Fowler et al., 2024). Despite the rainfall in low intensity, it was long-lasting and
52 widespread, resulting in large accumulated rainfall. Flooding from this event affected 1.3
53 million people, bringing severe human casualties and economic losses. One of the distinct
54 features of this rainfall event was closely associated with the remnant vortex originating from
55 typhoon Doksuri(2305), tropical storm Khanun(2306), unusual westward extended western
56 Pacific subtropical high (WPSH), and quasi-stationary cold dry air masses surrounding North
57 China on the west and north sides.

58 It is common for rainfall occurrence over North China due to strong water vapor supply
59 by tropical cyclones over the East China Sea and/or Southern China Sea (e.g., Ding,1978; Feng
60 and Cheng,2002; Yin et al.,2022c). Like the “96·8” heavy rainfall event (Sun et al.,2006; Bao
61 et al., 2024), the present persistent rainfall event was closely linked to two tropical storms of
62 Doksuri and Khanun. Note that the Doksuri weakened to a typhoon remnant vortex (typhoon-
63 low pressure) at this moment as it moved inland after landfalling, while the tropical storm
64 Khanun was in a fast-developing stage. The tropical storm Khanun and the typhoon remnant
65 vortex built a water vapor bridge, transporting a large amount of water vapor to North China
66 from the East China Sea. Previous studies (e.g., Hirata and Kawamura,2014; Gao et al.,2022;
67 Yang et al.,2017) pointed out that such large-scale weather conditions were favorable for heavy
68 rainfall generation.

69 In the last several decades, considerable attention was paid to the remote rainfall events
70 associated with tropical cyclones, and substantial progress has been made (e.g., Wang et al.,
71 2009; Xu et al.,2023a; Xu et al.,2023b; Lin and Wu,2021). Commonly, sufficient water vapor
72 provided by a tropical cyclone plays an important role in extreme rainfall over North China
73 (e.g., Rao et al.,2023; Xu et al.,2023b). Besides, many studies confirmed that the WPSH is
74 closely related to water vapor transportation and the spatial distribution of surface rainfall (e.g.,
75 Hu et al.,2019; Gao et al.,2022). Additionally, orographic forcing of the approaching warm and
76 moist unstable air plays a critical role in determining the location of convection initialization,



77 although sometimes orographic forcing played a small role compared to Typhoon's circulation
78 (Wang et al., 2009). Moreover, heavy rainfall can be generated by the complicated cloud
79 microphysical processes due to the interactions between tropical oceanic warm-moist and mid-
80 latitude cold-dry air masses (Wang et al., 2009; Xu and Li, 2017; Xu et al., 2021). Despite some
81 experiences gained, there are still large unexplained gaps in understanding the formation of
82 extreme rainfall (Meng et al., 2019). In this event, no highly organized strong convective system
83 was observed, and rainfall was featured by long duration, widespread coverage, and high
84 accumulation. Although operational forecasts gave reasonable results at that time, several
85 unique features emerged in this precipitation. Some unexplainable questions have been raised
86 after the persistent heavy rainfall event: (1) What mechanism(s) could account for the persistent
87 heavy rainfall? (2) What is the role of the unusual westward extended WPSH in governing the
88 rainfall over North China? Therefore, we are motivated to conduct the present modeling study
89 to answer those questions.

90 The rest of the paper is organized as follows. A detailed description of the main features
91 of extreme rainfall and synoptic-scale weather conditions is documented. Section 3 provides
92 detailed model configuration and verification against observations. We present a detailed
93 analysis of the extreme rainfall production in Section 4. The paper finishes with conclusions
94 and outlooks.

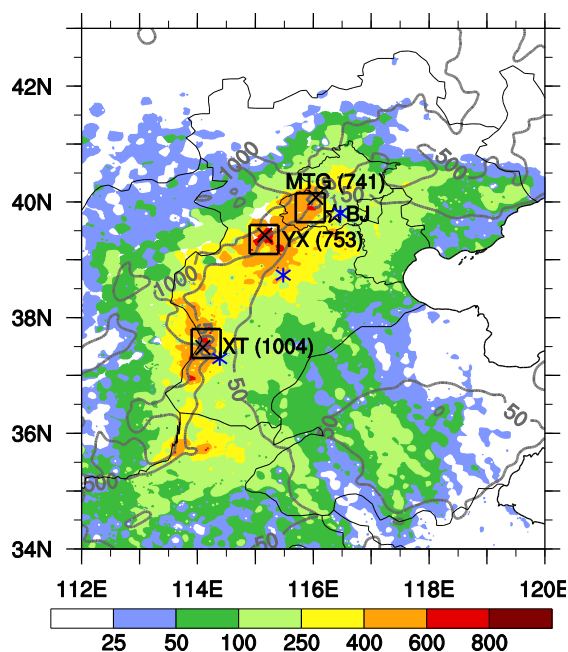
95 **2. Properties of rainfall and wind profiles**

96 ***2.1 Characteristics of rainfall***

97 Figure 1 shows the spatial distribution of 96-h accumulated rainfall from observations
98 during the period from 0000 UTC 29 July to 0000 UTC 2 August 2023, with the peak amount
99 of 1004 mm at Liangjiazhuang station near Xingtai, Hebei Province of North China.
100 Exceptionally long duration of rainfall is a notable feature of the event, with the longest duration
101 being 80 hours within the four days at some stations. The spatial distribution of heavy rainfalls
102 is consistent with the orography of the Yanshan Mountains on the north and the Taihang
103 Mountains on the south, suggesting that the heavy rainfall may be associated with the orography.
104 It should be emphasized that three rainfall cores, marked by Mentougou (MTG) in Beijing, and
105 Yixian (YX) and Xingtai (XT) in Hebei Province, correspond to the regions with large



106 topographic gradients (Fig. 1). Please refer to Li et al. (2024) for a detailed analysis of rainfall
107 fine features.



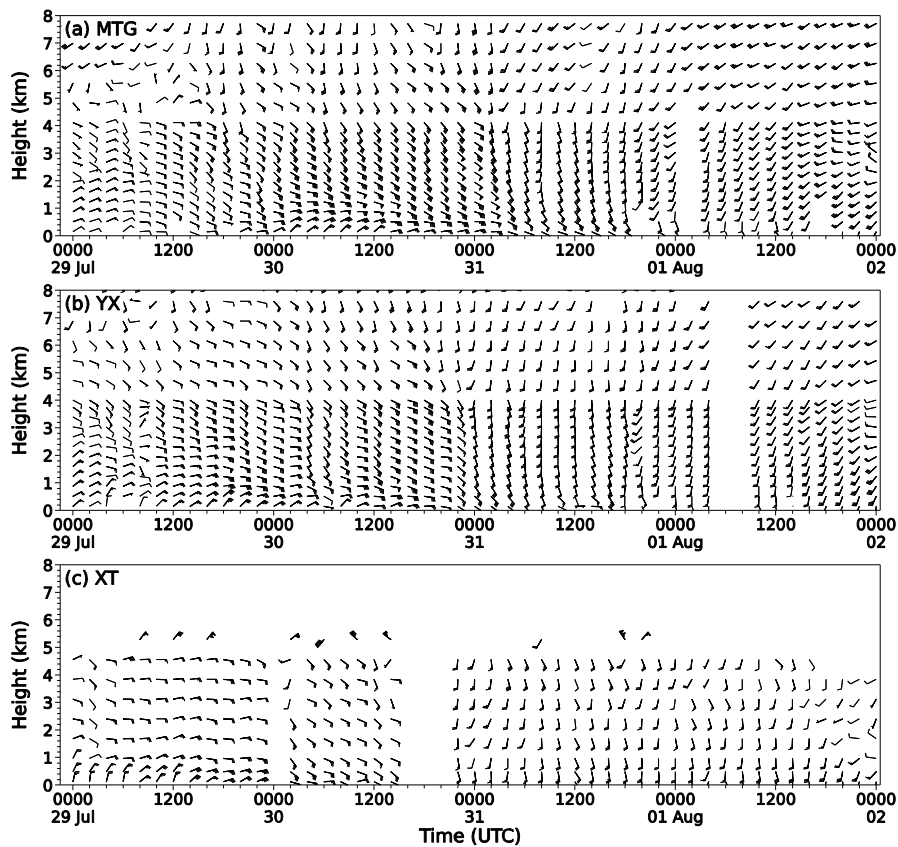
108
109 **Fig. 1** Spatial distribution of 96-h accumulated rainfall (mm, shadings) from the intensive
110 surface rain gauge observations during the period from 0000 UTC 29 July to 0000 UTC 2
111 August 2023; Gray contours denote orography from 50 m to 1000 m. Three rainfall cores in
112 Mentougou (MTG) in Beijing, and Yixian (YX) and Xiangtai (XT) in Hebei Province are
113 marked by squares, and the values in parentheses indicate the maximum accumulated rainfall
114 (marked by crisscross sign ×) for the regions, respectively. The blue asterisks (*) represent the
115 locations of wind profiler observational stations near the three rainfall cores. The start (☆) sign
116 indicates the location of Beijing (BJ) City. (Similarly for the rest of figures).

117 2.2 Wind profiles

118 The observed wind profiles near MTG, YX, and XT are shown in Fig. 2. Obvious temporal
119 variations in horizontal wind fields can be seen during the rainfall event. Taking the wind
120 profiles near MTG as an example (Fig. 2a), the easterly or southeasterly wind at the levels
121 below 4 km gradually increased from 2 m s^{-1} at 1200 UTC 28 to 24 m s^{-1} at 1200 UTC 30 July
122 2023. The easterly or southeasterly wind lasted to 0400 UTC 31 July 2023, turned southerly
123 except for near the ground, and then turned southwesterly near 0400 UTC 1 August 2023. After
124 0400 UTC 31 July, wind speed decreased significantly and then increased drastically. More



125 specifically, the wind speed decreased from 8 m s^{-1} to 2 m s^{-1} , then increased to 14 m s^{-1} near 1
126 km above the ground. However, opposite variations can also be seen above 4 km. One can see
127 that the horizontal wind shifted from southwesterly to southerly, then back to southwesterly.
128 Overall, the shift in wind direction and speed altered vertical wind shear, which directly affected
129 the development and organization of subsequent convection (Pucik et al., 2021). Similar
130 variations can also be found at YX and XT stations, although the timing of changes is not
131 synchronized (Fig. 2c,d). The variations proceeded from south to north, starting first at XT and
132 finally at MTG, as the typhoon moved from south to north.

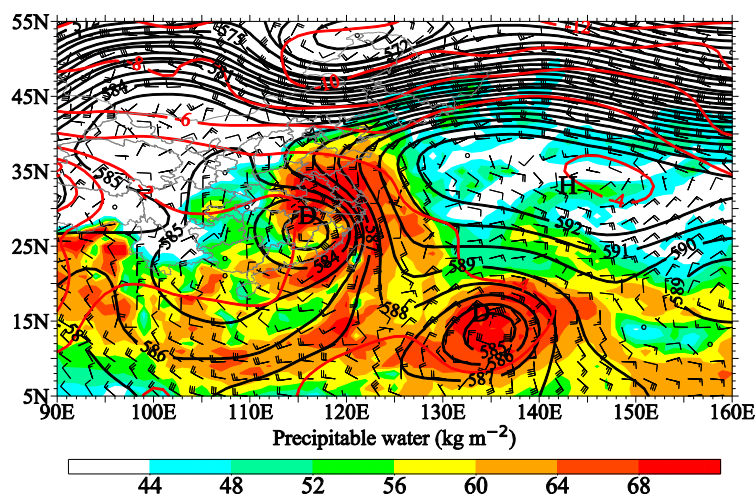


133
134 **Fig. 2** Temporal evolution of wind profile (a full barb is 4 m s^{-1}) from observations near (a)
135 MTG, (b) YX, and (c) XT during the period of 0000 UTC 29 July to 0000 UTC 2 August 2023.
136 Note only the wind profile below 5 km above the ground can be observed due to the limitation
137 of the instrumentation near Xingtai (XT). (see Fig. 1 their locations).



138 **2.3 Synoptic conditions on 28 July 2023**

139 Figure 3 displays a weather chart at 500 hPa at 1200 UTC 28 July 2023. One can see that
140 the large-scale flow patterns exhibited a coexistence of a remnant vortex originating from
141 typhoon Doksuri(2305)* and tropical storm Khanun(2306). The former weakened significantly
142 into a vortex at this time, while the latter was in the rapid development stage. Another important
143 weather system was the WPSH (denoted by the 588 isoline) with a square-head shape on its
144 western border. Clearly, a water vapor transportation passage was built due to the cyclonic
145 circulation of the tropical storm in combination with the anticyclonic circulation on the
146 southwest of the WPSH. As a result, central and North China was covered by high precipitable
147 water (PW) of over 68 mm. Similar patterns can be viewed at the level of 850 hPa (not shown).



148 **Fig. 3** Weather chart at 500 hPa at 1200 UTC 28 July 2023: Geopotential height (black-
149 contoured at 15 gpm intervals), temperature (red-contoured at 2°C intervals), wind barbs (a full
150 barb is 4 m s⁻¹), and precipitable water (kg m⁻², shadings).

152 **3. Model configuration and verification**

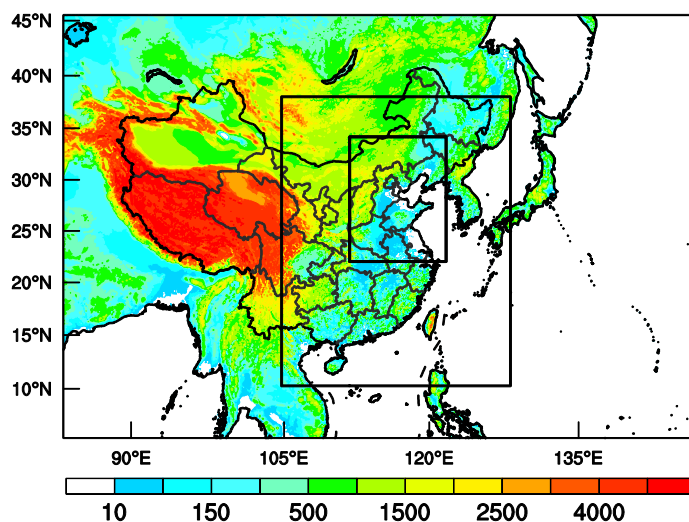
153 **3.1 Model description**

154 In this study, the persistent heavy rainfall event is reduplicated with the WRF model
155 version 4.1.3. The WRF model is configured in two-way nested grids of horizontal grid sizes
156 of 9 km, 3 km, and 1 km. Figure 4 displays the geographical coverage of the WRF model
157 domains, with the grid points of 901(nx)×601(ny), 973×1231, and 1231×1591 for the outer,

*The typhoon Doksuri(2305) weakened to a typhoon remnant vortex as it was passing through East China's Anhui Province. The China Meteorological Administration (CMA) stopped issuing updates on the Doksuri at 0300 UTC 29 July 2023. The remnant of Doksuri remained in a vortex in the lower troposphere, although its wind force diminished as it moved northward.



158 intermediate, and inner domains, respectively. The outermost domain (i.e., D01) is centered at
159 115°E, 35°N, and a total of 58 sigma levels is assigned in the vertical with the model top fixed
160 at 20 hPa. Since the rainfall is closely related to the spatial distribution of orography over North
161 China (Fig. 1), the Shuttle Radar Topography Mission (SRTM) high-resolution (90 m)
162 topographic data is employed in the present simulation. It should be noted that the model
163 vertical level distribution was carefully tested and has achieved good performance (Yin et al.,
164 2020; Yin et al.,2022a; Yin et al.,2018; Yin et al.,2022b). The WRF model physics schemes are
165 configured with the YSU scheme for the planetary boundary layer (Hong et al., 2006), the
166 revised MM5 Monin-Obukhov (Jimenez) scheme for the surface layer (Jiménez et al., 2012),
167 and the Unified Noah Land Surface Model (Tewari et al.,2004). The rapid radiative transfer
168 model (RRTM) (Mlawer et al.,1997) and the Dudhia scheme (Dudhia,1989) for longwave and
169 shortwave radiative flux calculations, respectively. The Kain-Fritsch cumulus parameterization
170 scheme (Kain,2004) is utilized for the outer two coarse-resolution domains but is bypassed in
171 the finest domain (i.e., D03). The Thompson-ensemble cloud microphysics scheme is applied
172 for explicit cloud processes (Thompson et al.,2008; Yin et al.,2022a).



173
174 **Fig. 4** The WRF model orography (m, shadings) and the nested model domains used for
175 simulations with the grid sizes of 9 km (D01), 3 km (D02), and 1 km (D03).

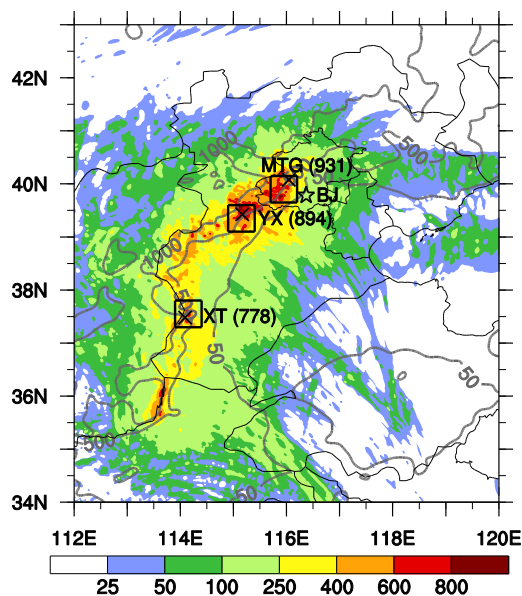
176 The WRF model is integrated for 108 hours, starting from 1200 UTC 28 July 2023, with
177 outputs at 6-min intervals. The model outputs in the first 12 h are considered as the spin-up
178 process and thus are not used for the present work. The initial and outermost boundary
179 conditions are interpolated from the final operational global analysis of 1-degree by 1-degree
180 data at 6-h intervals from the Global Forecasting System of the National Centers for



181 Environment Prediction (NCEP). In order to force large-scale fields consistent with the driving
182 fields, grid analysis nudging is activated by performing the Four-Dimension Data Assimilation
183 (FDDA) throughout the model integration (Bowden et al.,2012; Stauffer et al.,1991). The
184 innermost domain (i.e., D03) outputs are validated and used for further analysis, and the
185 outermost domain (i.e., D01) outputs are used to demonstrate weather-scale dynamical and
186 thermal features. Wind profiler and surface hourly observations are provided by the National
187 Meteorological Information Center (NMIC) of the China Meteorological Administration (CMA)
188 after strict quality control.

189 **3.2 Model verification**

190 Figure 5 shows the spatial distribution of 96-h accumulated rainfall from the simulation
191 during the period from 0000 UTC 29 July to 0000 UTC 02 August 2023. Generally speaking,
192 the WRF model replicates well the spatial distribution of heavy rainfall. The heavy rainfall belt
193 coinciding with the orography with three rainfall cores is reproduced well, and the simulated
194 extreme rainfall amount compares favorably to the observed. Note that the model produces a
195 peak 96-h accumulated rainfall of 778 mm over the XT region, while the maximum rainfall of
196 1004 mm was observed over the XT region. Despite the simulation underestimates rainfall over
197 this region, it captures the main features of rainfall over central and North China.

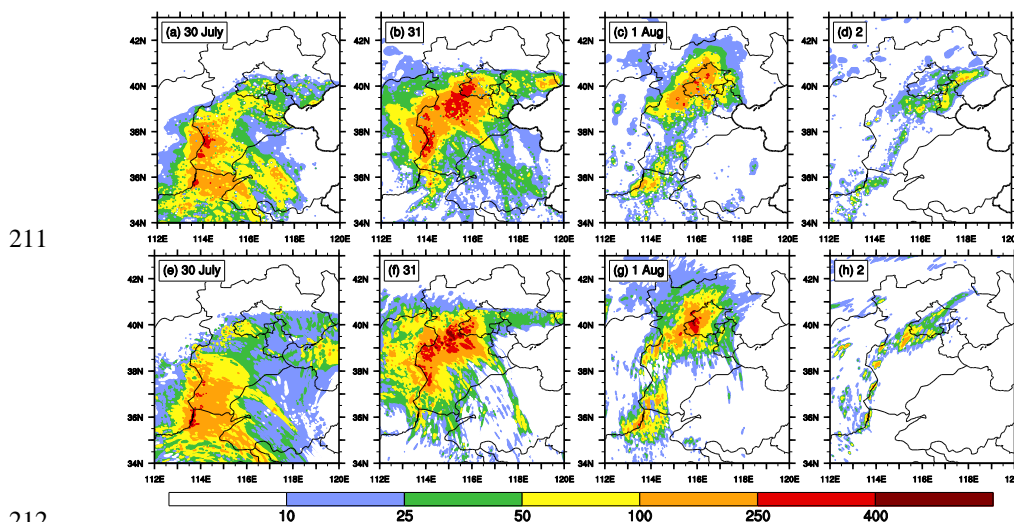


198
199

Fig. 5 Same as in Fig. 1 but for the simulated rainfall (mm, shadings).



200 Figure 6 compares the spatial distribution of daily rainfalls between observations and
201 simulations during the period from 0000 UTC 30 July to 0000 UTC 2 August 2023. From
202 observations, one can see that the daily rainfalls show obvious variations. On the first day (Fig.
203 6a), the rainfall occurred mainly in northern Henan and southern Hebei, on the east side of the
204 Taihang Mountains with the rainfall cores over 250 mm. On the next day (Fig. 6b), the rainfall
205 extended significantly northeastward, and a new strong rainfall core occurred, covering central
206 Hebei Province and southwest Beijing. On the third day (Fig. 6c), rainfall was significantly
207 reduced in both coverage and intensity, mainly occurring in Beijing and the surrounding areas.
208 On the fourth day (Fig. 6d), rainfall moved eastward and weakened rapidly. It is apparent that
209 the model reproduces the evolutions of the rainfall, with general characteristics that are similar
210 to the observed (Fig. 6e-h).

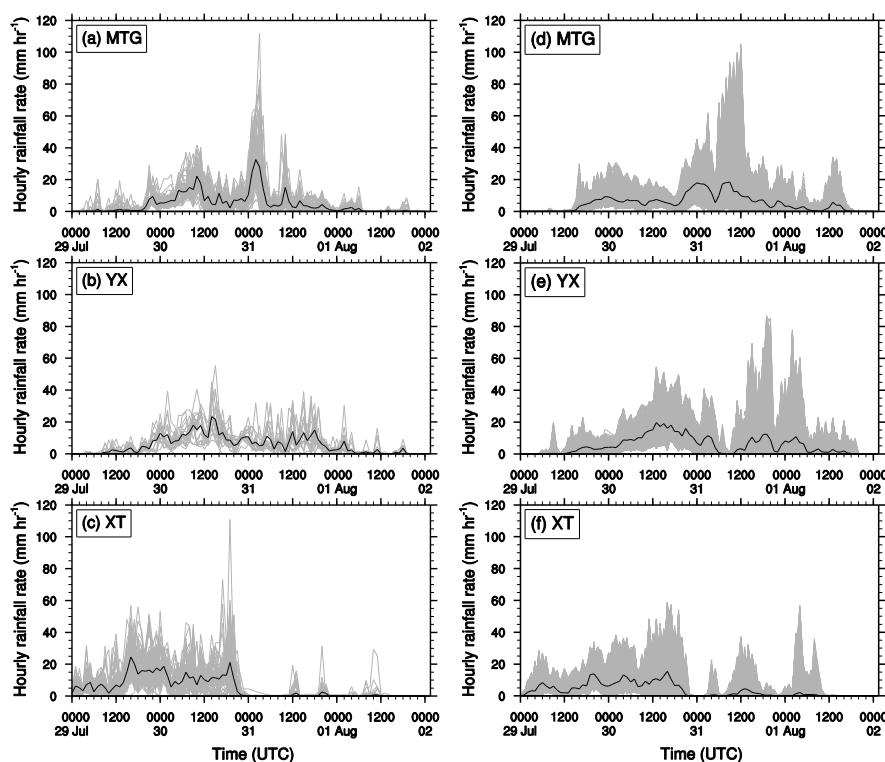


212 **Fig. 6** Spatial distribution of (a-d) observed and (e-h) simulated daily rainfall (mm) during the
213 period from 0000 UTC 30 July to 0000 UTC 2 August 2023.

215 Figure 7 compares the time series of hourly rainfall rates between the observed and
216 simulated over the MTG, YX, and XT regions. The rainfall event is characterized by long
217 duration, widespread coverage, and high accumulation. As has been mentioned above, the
218 rainfall extended from south to north, covering Henan, Hebei, and Beijing. The rainfall first
219 occurred in the XT region and ended near 0000 UTC 31 July 2023. As the rainfall moved
220 northeastward, both the MTG and YX regions occurred, ending nearly at 0000 UTC 2 August.



221 The observed timings of initiating and ending of the rainfall event are well replicated by the
222 WRF model. Besides, the observed peaks are reproduced, although there are some timing errors.
223 For example, the strongest rainfall occurred over the MTG region during the period from 0000
224 UTC to 0600 UTC 31 July. However, the simulated strongest rainfall has a 6-h lag, occurring
225 from nearly 0600 UTC to 1200 UTC 31 July. Overall, good agreements between the simulation
226 and observations are obtained in terms of the timing and location in the spatial distribution of
227 rainfall.

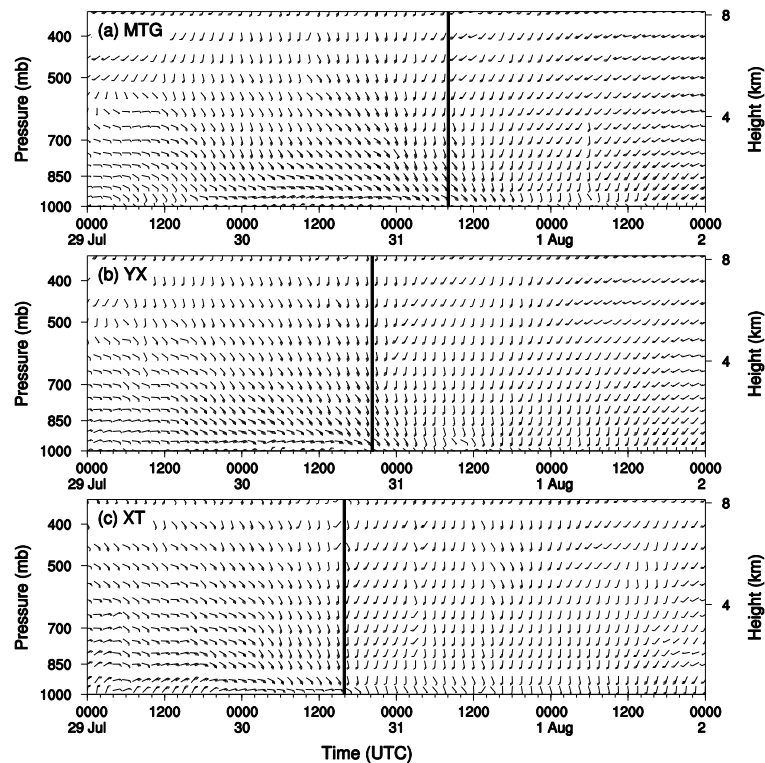


228
229 **Fig. 7** Time series of (a-c) rain gauge observations and (d-f) simulation hourly rainfall rates
230 (gray lines, mm hr^{-1}) for all stations/grid points over the (a, d) MTG, (b,e) YX, and (c,f) XT
231 regions during the period of 0000 UTC 29 July to 0000 UTC 02 August 2023. The black line
232 denotes the domain-averaged hourly rainfall rates of all stations (grid points) from observations
233 (simulations). (see Fig. 1 their locations).

234 The evolution of the simulated wind profile is presented in Fig. 8. Similar to the observed
235 (Fig. 2), the simulated easterly wind gradually increased from nearly 1200 UTC 29 July,
236 corresponding to the start of the precipitation (Fig. 6d-f). The horizontal wind experienced from



237 easterly to southerly except for near the ground, and then turned to southwesterly with wind
238 speed decreasing significantly. Overall, the variations of the simulated wind profile were
239 consistent with those observed, indicating that the WRF model well captured the main features
240 of the wind profile. Based on the wind profile and rainfall features, the simulated rainfall is
241 roughly divided into two stages. The shift moments (roughly marked by thick black lines) are
242 near at 0800 UTC 31, 2000 UTC 30, and 1600 UTC 30 July for the MTG, YX, and XT regions,
243 respectively.



244
245 **Fig. 8** Same as Fig. 2 but for the simulated. The black lines denote wind shift from southeasterly
246 to southerly/southwesterly over the levels in the low to middle troposphere, which roughly
247 divided the rainfall into two stages.

248 4. Characteristics of the rainfall event

249 4.1 Dominant dynamic processes for convection initialization

250 The evolution of dynamical and thermal systems of the rainfall event in the first stage is shown
251 in Fig. 9. Although only a remnant vortex remained over central China at this time, typhoon
252 Doksuri had an important influence on the WPSH when it was strong as a super typhoon.

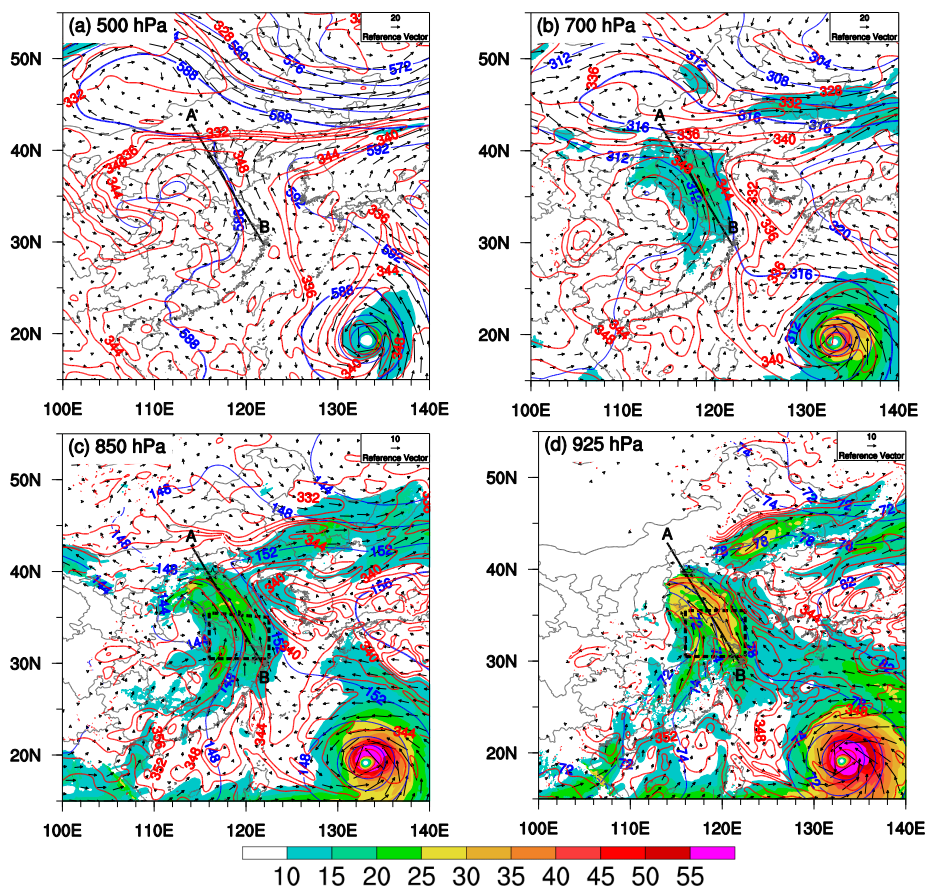


253 Several days before the rainfall event, the super typhoon Doksuri was close to the WPSH, and
254 the southwest WPSH edge was within the typhoon's outer region. Owing to the inflow mass
255 flux entering the typhoon region, and thus the southwest part of WPSH was severely destroyed
256 by typhoon Doksuri (Sun et al.,2015). As a result, the west boundary of the WPSH appeared to
257 an eastward retreat from 500 hPa to 850 hPa, showing an inclined vertical distribution on the
258 western boundary, especially from 700 hPa to 850 hPa. Capped by the inclined WPSH, water
259 vapor was mainly transported to North China through a passage nearly under 850 hPa which is
260 built by the typhoon remnant vortex and the tropical storm Khanun. At 500 hPa (Fig. 9a), the
261 WPSH (represented by the 588 isoline) covered a large part of eastern China, with an unusual
262 westward extension of the northwest corner to northwest China. The northwest corner extended
263 much further westward, compared to that before 12-h (Fig. 3). Similar patterns can be seen at
264 700 hPa (Fig. 7b), but the west boundary of WPSH (represented by the 316 isoline) retreated to
265 the East China Sea except for the northwest corner. At 850 hPa (Fig. 9c), the WPSH
266 (represented by the 156 isoline) completely retreated to the western Pacific, which was far away
267 from China.

268 The spatial distribution of the high PW was consistent with that of a large equivalent
269 potential temperature (θ_e) of 344K at 500 hPa, indicating that the 334K contour covered a
270 relatively warm and/or wet region (Fig. 9a). Most important, the boundary of the high PW
271 corresponded to the large value of the potential temperature gradient over 8K on the east side
272 and 12K on both north and west sides. Previous studies (e.g., Rao et al.,2023) proposed that the
273 heavy rainfall region was closely attributed to the distributions of θ_e . Although the warm and
274 moist conditions were favorable for precipitation, the unfavorable large-scale forcings explain
275 well why no deep convection was formed over this region (marked with a dashed-line box in
276 Fig. 9c,d). The convergence, resulting from changes in wind direction and wind speed, was
277 conducive to triggering convection. Consequently, the weak convergence led to weak lifting
278 and consequent precipitation. Since the convergence occurred at the junction of cold and warm
279 air masses, like a warm front rainfall, rainfalls were formed in low intensity but long duration
280 and widespread coverage. It is important to note that the spatial distribution of rainfall is usually
281 considered to be consistent with the western boundary of WPSH (i.e., the 588 isoline) at 500
282 hPa. However, the spatial distribution of rainfall in the present event is consistent with the dense
283 zone of θ_e , instead of the WPSH. Therefore, in addition to the isoline 588 at 500 hPa, the spatial



284 distribution of θ_e needs to be given more attention in future operational forecasts.



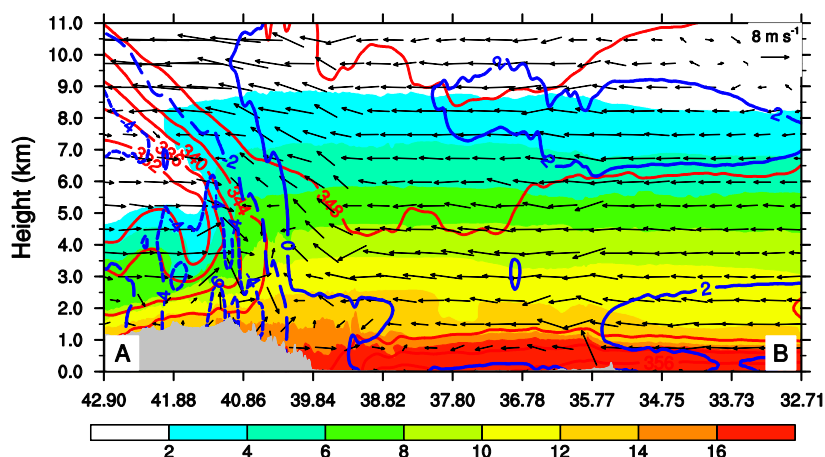
285 **Fig. 9** Spatial distribution of geopotential height (blue contoured at 40 gpm), equivalent
286 potential temperature (red contoured at 2K intervals, θ_e), wind bars (a full barb is 4 m s⁻¹), and
287 water vapor flux (g s⁻¹ cm⁻¹ hPa⁻¹, shadings) from the model D01 at 0000 UCT 30 July 2023:
288 (a) 500 hPa, (b) 700 hPa, and (c) 850 hPa, and (d) 925 hPa. The isolines of 588, 316, and 156
289 are bolded to represent the WPSH at 500 hPa, 700 hPa, and 850 hPa, respectively. The
290 convergence zone of southeast and southwest flows is marked by a dashed line box in panels
291 (c) and (d). The thick black line A–B denotes the locations for cross-section along the water
292 vapor transport pathway used in Fig. 10.

293 The warm and moist features over North China can also be seen from the cross-section
294 along line A–B as shown in Fig. 10. The western orography region was controlled by cold air
295 mass over the levels above 3.0 km. Under the conditions, significant equivalent potential
296 temperature gradients were established between the warm and cold air masses, similar to a
297 warm front. Meanwhile, owing to the blocking of orography below 1.3 km and the strong cold



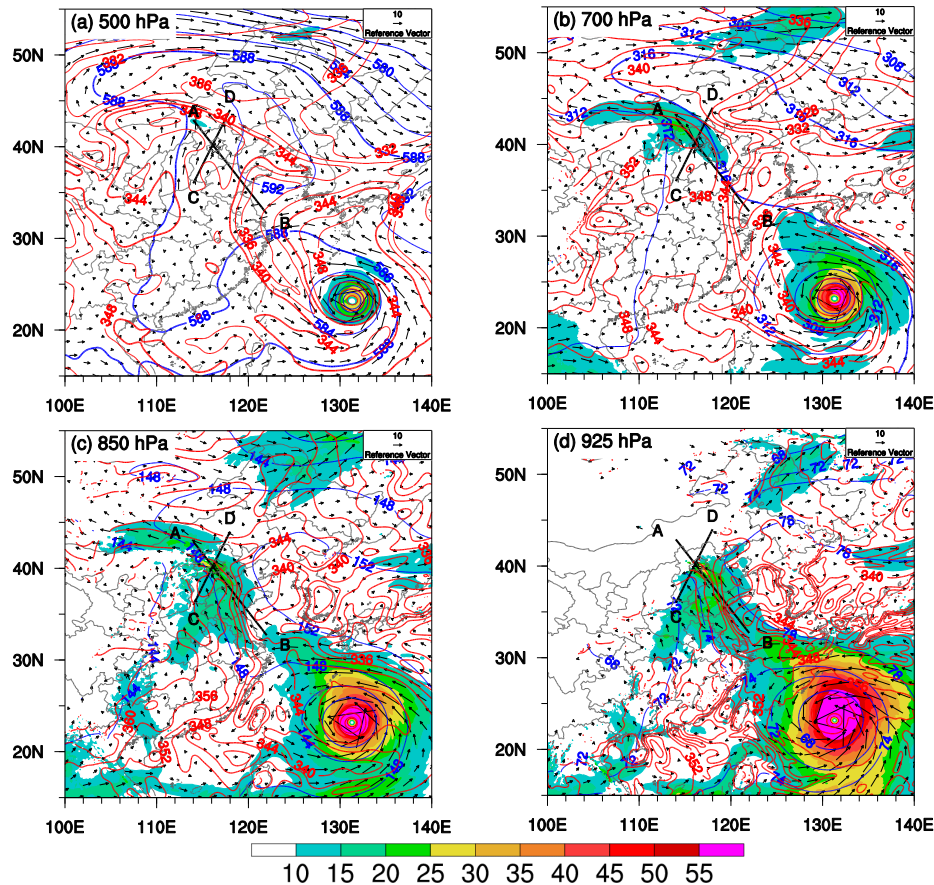
298 air mass above 3.0 km, only the southeasterly flows between 1.3 and 3.0 km above the sea level
299 can overpass the mountains. It should be noted that although the warm and moist southeasterly
300 flows were lifted by the orography, they could not move further upward to trigger convection
301 because of the local capped cold and dry air masses overhead. Consequently, convergence
302 mainly resulted from the changes in wind direction and wind speed led to upward motion. As
303 the warm and moist air was lifted, condensation occurred and thus generated precipitation. It
304 should be emphasized that the lifting was too weak to allow convection to be highly organized
305 (Fig. 10). For example, the updrafts in strong deep convective systems (e.g., Yin et al.,2020;
306 Yin et al.,2022c) are 5-10 times as large as the updrafts in the present event. Therefore, the weak
307 lifting was responsible for the rainfall in large coverage but low intensity. Besides, the
308 continuous and stable water vapor supply was another favorable factor for the precipitation.

309 Also from Fig. 10, one can see that North China was surrounded by warm dry air masses
310 on the east side and cold dry air masses on both north and west sides. More specifically, the air
311 mass at the levels above 1 km on the east side was over 3°C warmer than surrounding regions,
312 but the water vapor mixing ratio (q_v) was less than 14 g kg⁻¹ (humidity was less than 70%)
313 because this region was controlled by the WPSH. The warm-dry cap overhead explains well
314 the absence of convection and rainfall over this region (cf. Figs. 5 and 6). On the north and west
315 sides, the air masses were dry with q_v less than 2 g kg⁻¹. The air was over 3°C colder than the
316 surrounding region except for the air near the ground. Note that warm air near the ground might
317 be associated with radiative heating from the ground. Capped by the cold and dry air overhead
318 explains why convection could not be advanced over the mountains.



319
320 **Fig. 10** Vertical cross-section along line A–B given in Fig. 9 of temperature deviations (blue-
321 contoured at 2°C intervals) from their level-averaged values in the cross-section, equivalent
322 potential temperature (red-contoured at 4K intervals), water vapor mixing ratio (q_v , g kg^{-1} ,
323 shadings), and in-plane flow vectors (vertical motion amplified by a factor of 20) at 0000 UCT
324 30 July 2023, respectively. Gray shadings denote terrain.

325 In the second stage (Fig. 11), obvious differences in dynamical and thermal processes can
326 be viewed, compared to those in the first stage (cf. Fig. 9). At 500 hPa (Fig. 11a), the WPSH
327 further expanded westward with its western border reaching western China. It should be
328 emphasized that the southwest part of WPSH was severely damaged by the rapid intensification
329 of Khanun into a super typhoon. Meanwhile, as the trough deepened over northeastern China,
330 cold air from the north poured southward. Consequently, a north-south orientated θ_e dense zone
331 was established over eastern China. Similar patterns in θ_e and horizontal wind field can be seen
332 at 700 hPa (Fig. 11b). However, the WPSH (represented by the 316 isoline) was further
333 disrupted as the Khanun continued to intensify, appearing that the WPSH retreated to the East
334 China Sea except for the northwest corner. The north-south orientated θ_e dense zone greatly
335 prevented water vapor from transporting to North China above 850 hPa, and thus water vapor
336 was mainly transported to North China by a shallow southeasterly flow near the ground (Fig.
337 11c,d). Consequently, the water vapor flux was significantly reduced (Fig. 12a). Besides, North
338 China was dominated by southerly flows over levels above 500 hPa, and thus mid-tropospheric
339 wind shear was significantly enhanced.

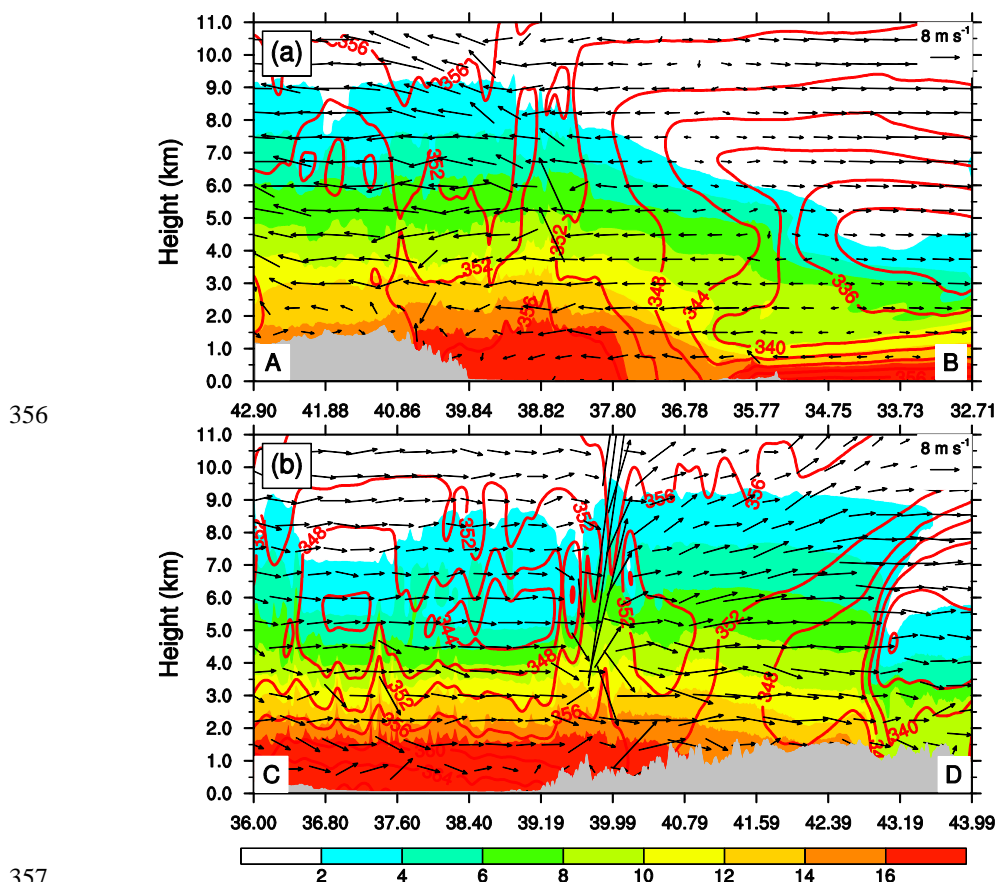


340 **Fig. 11** Same as Fig. 9 but for 0800 UTC 31 July 2023. Thick black lines A–B and C–D denote
341 the locations for the cross-section in Fig. 12.

342 As addressed above, variations in environmental conditions caused consequent rainfall
343 changes in nature. Especially, the shift in the wind field brought changes in thermodynamic
344 processes and water vapor sources. Before the wind shift (Figs. 9 and 10), water vapor was
345 mainly from the East China Sea associated with the cyclonic circulation of the typhoon remnant
346 vortex and the tropical storm Khanun and southeasterly flow below 925 hPa. After the shift,
347 water vapor flux was significantly reduced from both southwesterly and southeasterly flows
348 (Fig. 11). Under the framework, convections were triggered by orographic blocking and lifting
349 of southerly/southwesterly flows as convective instability air approached orography (Fig. 12).
350 Unlike in the first stage, convections were further developed over mountains northward,
351 forming deep convections (Fig. 12b). One of the reasons is that the cold air on the north side



352 moved northward. Comparatively speaking, the convections in the second stage are much
353 stronger and deeper than those in the first stage. Consequently, the rainfall intensity is increased,
354 compared to those in the first stage (Figs. 7d,e). The weak convections may be attributed to the
355 reduced water vapor supply during this period.



356
357
358 **Fig. 12** Vertical cross-sections along lines (a) A–B and (b) C–D given in Fig. 11 of equivalent
359 potential temperature (θ_e , red-contoured at 4K intervals), water vapor mixing ratio (q_v , g kg^{-1} ,
360 shadings), and in-plane flow vectors (vertical motion amplified by a factor of 10) at 0800 UCT
361 31 July 2023. Gray shadings denote terrain.

362 4.2 Moisture budget

363 The shift in wind direction and speed implies a change in water vapor source and rainfall
364 properties (Fig. 13). As stated above, water vapor was mainly from the East China Sea
365 associated with the cyclonic circulation of typhoon Khanun before the wind shift, and was



366 fueled by the southeasterly flow below 925 hPa. After the shift, the water vapor supply was
367 significantly reduced from both southwesterly and southeasterly flows. Figure 13 shows the
368 time-height cross-sections of moisture flux across eastern, southern, western, and northern
369 boundaries and total lateral boundary moisture flux for the MTG region. The moisture flux is
370 calculated as

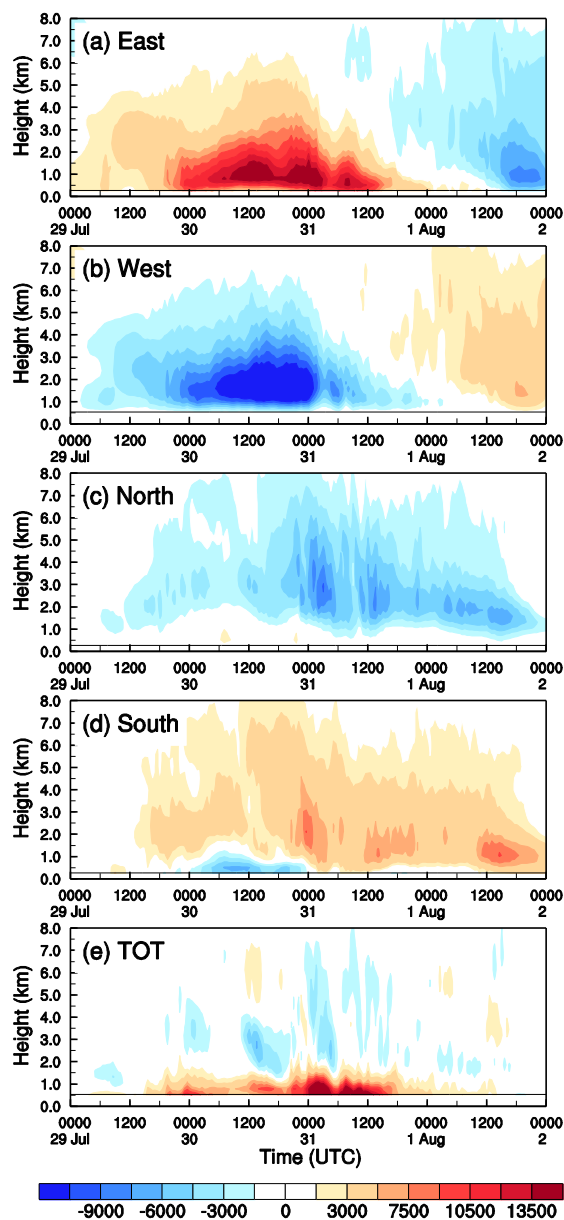
$$371 \quad QFlux = \int_0^L q_v \vec{v} dl .$$

372 Here, $QFlux$ is moisture flux across one of the four boundaries, and q_v , \vec{v} , and L are water
373 vapor mixing ratio, wind vector, and the length of the boundary, respectively. The TOT is a
374 summation of the $QFlux$ s from the four boundaries by taking inward(outward) as
375 positive(negative).

376 One can see that the MTG region experienced vigorous lower-to-middle level inward
377 (outward) moisture fluxes across their eastern and southern (western and northern) boundaries.
378 For the eastern boundary (Fig. 13a), the inward moisture flux began to increase gradually from
379 0000 UTC 29 July, with the maximum values over $13,500 \text{ kg kg}^{-1} \text{ m}^2 \text{ s}^{-1}$ occurring between
380 1200 UTC 30 and 0000 UTC 31 July 2023. Then, the inward flux moisture decreased rapidly
381 and even transformed to the outward flux at 0000 UTC 1 August 2023. The inward moisture
382 flux was mainly concentrated below 3 km above the sea level because upper levels were capped
383 by the warm dry air masses associated with the WPSH (cf. Figs. 9 and 10). However, owing to
384 weak lifting over, most of the water vapor flowed out through the western boundary (Fig. 13b).
385 Meanwhile, part water vapor was transported in this region from the southern boundary except
386 for the lower levels during 0000 UTC 30 to 0000 UTC 31 July 2023 (Fig. 13d). The outward
387 flow water vapor resulted from the northeasterly around flow due to the blocking of the Yanshan
388 Mountains. Similar patterns can be seen in the northern boundary with almost the same outward
389 water vapor flux (Fig. 13c). The temporal evolution of the water vapor flux across the eastern
390 boundary is consistent with that of rainfall over this region (Figs. 13a and 7d), suggesting that
391 rainfall formation was dominated by the inward of water vapor from the eastern boundary.
392 Overall, the inward net moisture fluxes were concentrated in the lower troposphere between 0.5
393 km and 1.5 km (Fig. 13e), suggesting that most of the water vapor was consumed at this layer



394 by condensation. Despite the high water vapor flux, the water vapor-rich layer is too thin (nearly
395 1 km) to be favorable for the formation of heavy rainfall. Similar patterns can be found over
396 both YX and XT regions (not shown), although there were temporal and quantitative differences.



397
398 **Fig. 13** Time-height cross sections of moisture fluxes ($\text{kg kg}^{-1} \text{m}^2 \text{s}^{-1}$) through the (a) eastern,
399 (b) western, (c) northern, and (d) southern boundaries of the MTG region in Fig. 1; (e) TOT
400 provides the total net moisture flux of all boundaries.



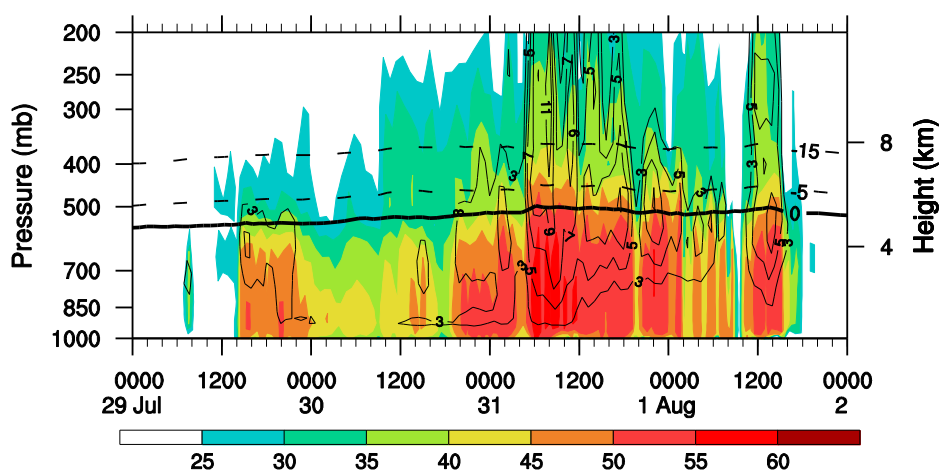
401 In the second stage, the north-south orientated θ_e dense zone greatly prevented water vapor
402 from being transported to North China by southeasterly flows from the East China Sea, and
403 thus water vapor was mainly transported to North China across the south boundary (Figs. 13b,d).
404 Unlikely, the water vapor was mainly provided by southeasterly(southwesterly) flow
405 below(above) 500 hPa. Note that the water vapor flux amount was significantly reduced (Fig.
406 13). Despite the thickening of the water vapor flux layer associated with the
407 southerly/southwesterly flows, the water vapor flux is much less, compared to the first stage.
408 Therefore, the wind shift had strong effects on the reduction in water vapor flux and consequent
409 rainfall over North China. The same results can also be obtained in the YX and XT regions (not
410 shown). It is worth emphasizing that strong hourly rainfalls occurred during the wind shift
411 period (cf. Figs. 2, 7, and 8), suggesting that the changes in wind direction enhanced wind shear
412 and thus promoted the development of convections and consequent precipitation under moisture
413 and instability conditions (Chen et al.,2015; Rotunno et al.,1988; Schumacher and Rasmussen,
414 2020). Therefore, it is important to pay special attention to environmental wind alterations in
415 future remote rainfall forecasts.

416 **4.3 Properties of convection**

417 Figure 14 shows the temporal evolution of maximum upward motion and radar reflectivity
418 over the MTG region during the rainfall period from 0000 UTC 29 to 0000 UTC 2 August 2023.
419 In the first stage (i.e., before 0800 31 July), most of the maximum updrafts were almost less
420 than 3 m s^{-1} . Owing to the weak updrafts, the storm did not stretch as high as typical convective
421 systems over North China, with hydrometeors concentrated on the levels with temperature
422 above 0°C (Fig. 14a). As addressed above (Fig. 10), weak updrafts were attributed by the
423 unfavorable large-scale forcings. The vertical distribution of hydrometeor indicates that the
424 warm rain processes were dominant in the persistent rainfall event. The result is consistent with
425 the water vapor consumed layer between 0.5 km and 1.5 km (Fig. 13e). Unlikely, the maximum
426 updraft was over 11 m s^{-1} in the second stage (i.e., after 0800 31 July), which is much stronger
427 than that in the first stage (Fig. 14). Correspondingly, the radar reflectivity penetrated through
428 the 0°C level with a cloud top exceeding 12 km, indicating that both warm and cold rain
429 processes were active in this stage. Correspondingly, the intensity of hourly rainfall increased



430 significantly, with the maximum value exceeding 100 mm (Fig. 7d). Comparatively speaking,
431 there are larger strong convective areas in the second than those in the first stage. The same
432 features were also found in the regions of YX and XT (not shown). Unlike the usual short-
433 duration heavy rainfall in North China (Mao et al., 2018; Xia and Zhang, 2019; Yin et al., 2022b),
434 this precipitation was mainly dominated by warm cloud processes (Fig. 14). As addressed above,
435 the weak updrafts but warm-moist air were responsible for persistent rainfall but low intensity.
436 A detailed analysis of cloud microphysical processes for this event will be given in a
437 forthcoming study, in which all microphysical source and sink terms will be explained.



438
439 **Fig. 14** Time-height cross-section of domain maximum radar reflectivity (dBZ, shadings) and
440 upward motion (contoured at 2 m s^{-1}) taken from MTG region during the period from 0000
441 UTC 29 to 0000 UTC 2 August 2023. The isothermal lines denote the 0°C (the melting layer),
442 -5°C , and -15°C levels, respectively.

443 5. Conclusions and outlook

444 In this study, we examined the convective initiation and subsequent persistent heavy
445 rainfall over North China during the period from 29 July to 2 August 2023 with observations
446 and simulations with the WRF model. From observations, the rainfall was featured by long
447 duration and widespread coverage but low intensity, like a warm front rainfall. Firstly, the
448 persistent heavy rainfall event was reproduced by the WRF model. Further analysis based on
449 the simulations shows that this persistent precipitation was caused by a combination of a
450 remnant vortex originating from typhoon Doksuri(2305), the tropical storm Khanun(2306), the



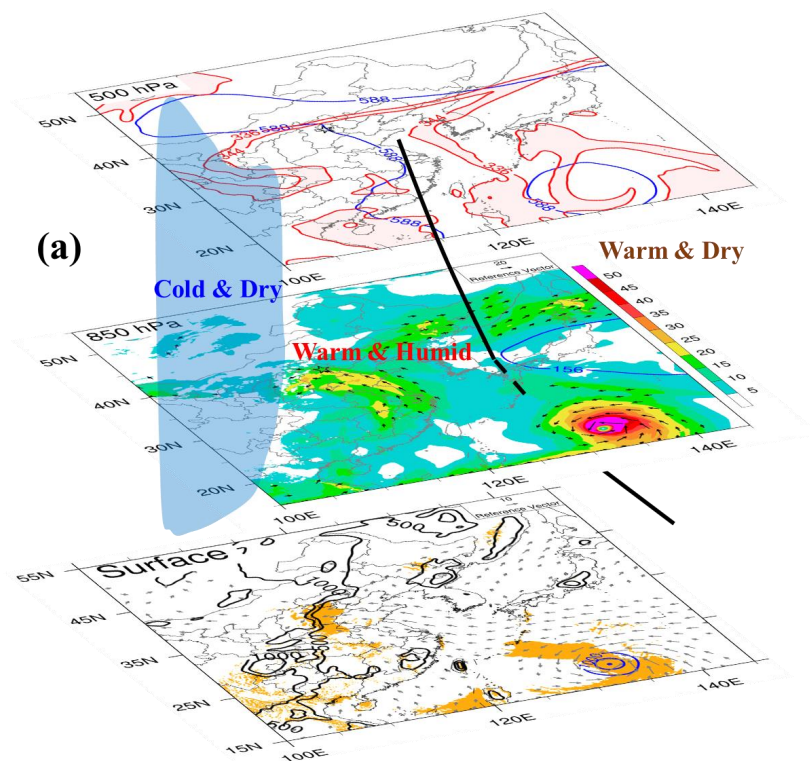
451 west Pacific subtropical high (WPSH) with an unusual westward extension of the northwestern
452 corner, and stable cold dry air from over northern China.

453 According to the simulated wind profiles and rainfall features, the persistent heavy rainfall
454 event was divided into two stages. Figure 15 summarizes the synoptic-scale forcings and
455 possible dynamic mechanisms for the persistent heavy rainfall. In the first stage (Fig. 15a), a
456 water vapor transportation passage was built by a typhoon remnant vortex and a tropical storm
457 Khanun, providing a stable warm moist water vapor supply. Several days before the rainfall
458 event, the southwestern WPSH was within the typhoon Doksuri's outer region, and thus the
459 southwestern WPSH was destroyed by the tropical storm Doksuri. It appears that the west
460 boundary of the western Pacific subtropical high (WPSH) retreated eastward from 500 hPa to
461 850 hPa, showing an inclined vertical distribution on the western boundary, especially from 700
462 hPa to 850 hPa. Capped by the inclined WPSH, water vapor was mainly transported to North
463 China through a water vapor passage under nearly 850 hPa (Fig. 10). Although the warm and
464 moist regions were favorable for precipitation over North China, organized strong convective
465 systems were seldom because of the absence of unfavorable large-scale conditions. At the same
466 time, the orography in the west of North China was controlled by dry cold air mass over levels
467 above 3.0 km. Owing to the blockings of orography below 1.3 km and the strong cold air mass
468 above 3.0 km, only the southeasterly flows between 1.3 and 3.0 km above the sea level can
469 overpass the mountains. Although the warm and moist southeasterly flows were lifted by the
470 orography, they could not go further upward to trigger convections because of the locally
471 capped cold and dry air masses overhead. Under the conditions, significant equivalent potential
472 temperature gradients were established between the warm and cold air masses, similar to a
473 warm front. Consequently, convergence mainly resulted from the changes in wind direction and
474 wind speed led to upward motion. As the warm and moist air was lifted, condensation occurred
475 and thus generated precipitation. However, the lifting was too weak to allow convection to be
476 highly organized (Fig. 14), leading to the rainfall in low intensity but large coverage. Besides,
477 the continuous and stable transportation of water vapor provided by tropical storm Khanun
478 ensured stable precipitation over a long period of over 80 h. Therefore, this event shows similar
479 rainfall features to those of a warm front rainfall with a long duration and widespread coverage

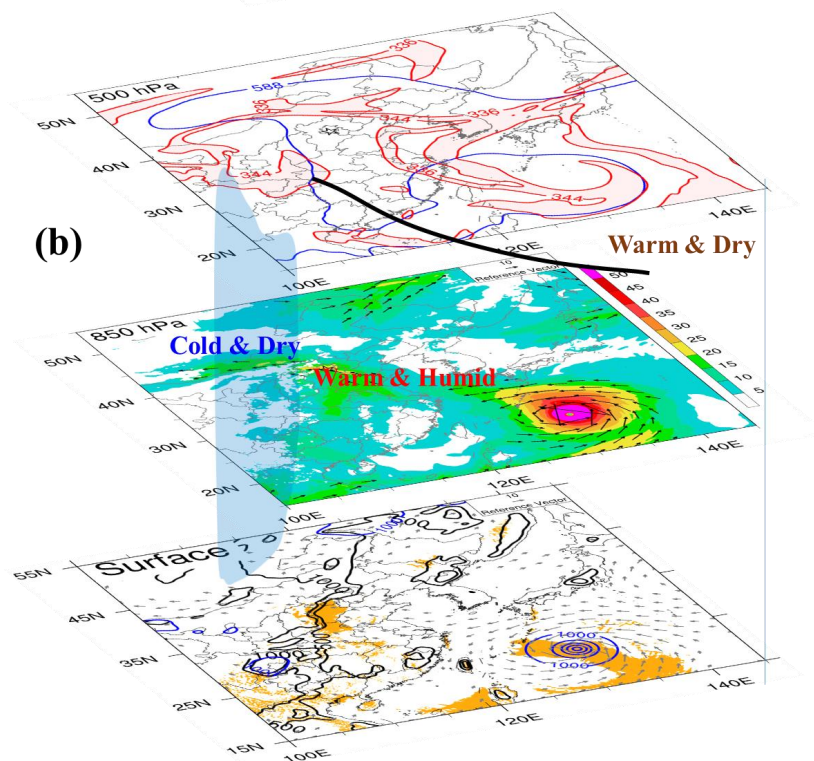


480 but low intensity.

481 In the second stage (Fig. 15b), the WPSH further expanded westward at 500 hPa, with its
482 western border reaching western China. However, the southwest part of WPSH was further
483 damaged by the rapid intensification of Khanun into a super typhoon. Consequently, the
484 embedded warm-dry cover associated with the tilted WPSH was significantly thinned, favoring
485 convective development. Meanwhile, as the trough deepened over northeastern China, cold air
486 from the north poured southward. Consequently, a north-south-orientated equivalent potential
487 temperature (θ_e) dense zone was established over eastern China, which greatly prevented water
488 vapor from being transported to North China (Fig. 12a). However, owing to the clockwise
489 rotated southeasterly flow, a deep southerly (southwesterly) flow was built over North China.
490 Convections were triggered by orographic blocking and lifting of southerly/southwesterly flows
491 as convective instability air approached orography. Unlike the first stage, the convections were
492 further developed over mountains northward, forming deep convections. It should be noted that
493 the northward-moved cold air on the north side was another favorable condition. Therefore, the
494 convections in the second stage are much stronger and deeper than those in the first stage,
495 although water vapor flux is smaller than in the second period. Consequently, the rainfall
496 intensity is increased, compared to that in the first stage. Correspondingly, both warm and cold
497 rain processes were active in the second stage, while warm rain processes were dominant in the
498 first stage.



499



500



501 **Fig. 15** (a) Three-dimensional diagram of the mechanisms for the persistent heavy in the first
502 stage. Several distinct synoptic systems, including the tropical storm Khanun(2306), a
503 remnant vortex originating from the typhoon Doksuri(2305), quasi-stationary cold dry air
504 masses, and an abnormal western Pacific subtropical high (WPSH) with inclined vertical
505 distribution on the western boundary (thick black line). Blue lines marked with 588 and 156
506 represent the WPSH at 500 hPa and 850 hPa, respectively. Red lines denote the spatial
507 distribution of equivalent potential temperature (θ_e) dense zone between 336 K and 344K. At
508 850 hPa, black arrows indicate jets with wind speed over 12 m s^{-1} , and shadings denote water
509 vapor flux. Orange shadings imply 96-h accumulated rainfall over 200 mm; blue contours
510 denote sea level pressure; gray arrows denote surface (i.e., $z = 10 \text{ m}$) horizontal wind with
511 wind speed over 5 m s^{-1} , and black contours indicate orography (m). (b) Same as (a) but for
512 rainfall in the second stage.

513

514 In this study, we have gained principal results of the persistent heavy rainfall event. It is
515 important to note that the spatial distribution of rainfall is usually considered to be consistent
516 with the western boundary of WPSH (i.e., the 588 isoline) at 500 hPa. In the present event, the
517 spatial distribution of rainfall is consistent with the dense zone of θ_e , rather than the western
518 boundary of WPSH. Therefore, in addition to the 588 isoline, the spatial distribution of θ_e needs
519 to be given more attention in future operational forecasts. Besides, we should give weight to
520 environmental wind shifts, which may lead to changes in convections and the nature of
521 consequent precipitation. Although reasonable dynamic mechanisms for the present persistent
522 heavy rainfall have been proposed, there are still several questions that need to be answered.
523 Among those, more work is required to understand detailed cloud and precipitation processes.
524 In addition, diagnostic and budget analyses will be conducted to understand how the orography
525 facilitates the generation of the rainfall belt with three rainfall cores along the mountains.
526 Nevertheless, the concept of synoptic-forcing-based forecasting is discussed as it might apply
527 to a broader spectrum of forecast events than just over North China.

528

529 **Code and data availability**

530 The source code of the Weather Research and Forecasting model (WRF v4.1.3) is available at
531 <https://github.com/wrf-model/WRF/releases> (last access 1 August 2024). The National Centers



532 for Environmental Prediction (NCEP) Global Forecast System one-degree final analysis data at
533 6 h intervals used for the initial and boundary conditions for the specific analyzed period can
534 be downloaded at <https://rda.ucar.edu/datasets/d083002/> (last access 1 August 2024). Modified
535 WRF model codes and all the data used in this study are available from the authors upon request.

536

537 **Author contributions**

538 Conceptualization: JY, JS, and XL; methodology: JY and JS; data curation: JY and FL; writing
539 – original draft preparation: JY, and FL; writing – review and editing: JY, ML, RX, XB, and JS;
540 project administration: XL; funding acquisition: JY and XL. All authors have read and agreed
541 to the published version of the paper.

542

543 **Competing interests**

544 The contact author has declared that none of the authors has any competing interests.

545

546 **Acknowledgments**

547 The authors acknowledge the use of the NCAR Command Language (NCL) in the preparation
548 of figures.

549

550 **Financial support**

551 This study is jointly supported by the National Key R&D Program of China
552 (2022YFC3003903), National Natural Science Foundation of China (42075083), Open Project
553 Fund of China Meteorological Administration Basin Heavy Rainfall Key Laboratory
554 (2023BHR-Z03), and the Development Foundation of Chinese Academy of Meteorological
555 Sciences (2019KJ026).



556

References

- 557 Bao, X., J. Sun, J. Yin, X. Gao, F. Li, X. Liang, H. Gu, R. Xia, M. Li, C. Wu, and J. Feng, 2024: What Caused
558 the Differences between “23·7” and “96·8” Extreme Rainfall Events in North China under a Similar
559 Synoptic Background? *Journal of Meteorological Research*, **88**, 1-19, doi:10.1007/s13351-024-3192-0.
- 560 Bowden, J. H., T. L. Otte, C. G. Nolte, and M. J. Otte, 2012: Examining Interior Grid Nudging Techniques Using
561 Two-Way Nesting in the WRF Model for Regional Climate Modeling. *J. Clim.*, **25**, 2805-2823,
562 doi:10.1175/JCLI-D-11-00167.1.
- 563 Chen, Q., J. Fan, S. Hagos, W. I. Gustafson Jr, and L. K. Berg, 2015: Roles of wind shear at different vertical
564 levels: Cloud system organization and properties. *Journal of Geophysical Research: Atmospheres*, **120**,
565 6551-6574, doi:https://doi.org/10.1002/2015JD023253.
- 566 Ding, Y., 1978: A case study on the excessively severe rainstorm in Honan province, early in August, 1975.
567 *Scientia Atmospherica Sinica*, **2**, 276-289. (in Chinese).
- 568 Dudhia, J., 1989: Numerical Study of Convection Observed during the Winter Monsoon Experiment Using a
569 Mesoscale Two-Dimensional Model. *Journal of the Atmospheric Sciences*, **46**, 3077-3107,
570 doi:10.1175/1520-0469(1989)046<3077:NSOCOD>2.0.CO;2.
- 571 Feng, W., and L. Cheng, 2002: Nonhydrostatic numerical simulation for the "96.8" extraordinary rainstorm and
572 the developing structure of mesoscale system, **16**, 423-440.
- 573 Fowler, H. J., S. Blenkinsop, A. Green, and P. A. Davies, 2024: Precipitation extremes in 2023. *Nature Reviews*
574 *Earth & Environment*, **5**, 250-252, doi:10.1038/s43017-024-00547-9.
- 575 Gao, Z., J. Zhang, M. Yu, Z. Liu, R. Yin, S. Zhou, L. Zong, G. Ning, X. Xu, Y. Guo, H. Wei, and Y. Yang, 2022:
576 Role of Water Vapor Modulation From Multiple Pathways in the Occurrence of a Record-Breaking Heavy
577 Rainfall Event in China in 2021. *Earth and Space Science*, **9**, e2022EA002357,
578 doi:https://doi.org/10.1029/2022EA002357.
- 579 Hirata, H., and R. Kawamura, 2014: Scale interaction between typhoons and the North Pacific subtropical high
580 and associated remote effects during the Baiu/Meiyu season. *Journal of Geophysical Research:*
581 *Atmospheres*, **119**, 5157-5170, doi:https://doi.org/10.1002/2013JD021430.
- 582 Hong, S.-Y., J. Dudhia, and S.-H. Chen, 2004: A revised approach to ice microphysical processes for the bulk
583 parameterization of clouds and precipitation. *Monthly Weather Review*, **132**, 103-120, doi:10.1175/1520-



- 584 0493(2004)132<0103:ARATIM>2.0.CO;2.
- 585 Hu, G., M.-H. Lu, D. Reynolds, H.-K. Wang, X. Chen, W.-C. Liu, F. Zhu, X.-W. Wu, F. Xia, M.-C. Xie, X.-N.
586 Cheng, K.-S. Lim, B.-P. Zhai, and J. Chapman, 2019: Long-term seasonal forecasting of a major migrant
587 insect pest: the brown planthopper in the Lower Yangtze River Valley. *J. Pest Sci.*, **92**, doi:10.1007/s10340-
588 018-1022-9.
- 589 Jiménez, P. A., J. Dudhia, J. F. González-Rouco, J. Navarro, J. P. Montávez, and E. García-Bustamante, 2012: A
590 Revised Scheme for the WRF Surface Layer Formulation. *Monthly Weather Review*, **140**, 898-918,
591 doi:10.1175/MWR-D-11-00056.1.
- 592 Kain, J. S., 2004: The Kain–Fritsch Convective Parameterization: An Update. *Journal of Applied Meteorology*,
593 **43**, 170-181, doi:10.1175/1520-0450(2004)043<0170:TKCPAU>2.0.CO;2.
- 594 Li, M., J. Sun, F. Li, C. Wu, R. Xia, X. Bao, J. Yin, and X. Liang, 2024: Precipitation Evolution from Plain to
595 Mountains during the July 2023 Extreme Heavy Rainfall Event in North China. *Journal of Meteorological*
596 *Research*, **38**, 1-17, doi:10.1007/s13351-024-3182-2.
- 597 Lin, Y.-H., and C.-C. Wu, 2021: Remote Rainfall of Typhoon Khanun (2017): Monsoon Mode and Topographic
598 Mode. *Monthly Weather Review*, **149**, 733-752, doi:https://doi.org/10.1175/MWR-D-20-0037.1.
- 599 Mao, J., F. Ping, L. Yin, and X. Qiu, 2018: A Study of Cloud Microphysical Processes Associated With Torrential
600 Rainfall Event Over Beijing. *Journal of Geophysical Research: Atmospheres*, **123**, 8768-8791,
601 doi:https://doi.org/10.1029/2018JD028490.
- 602 Meng, Z., F. Zhang, D. Luo, Z. Tan, J. Fang, J. Sun, X. Shen, Y. Zhang, S. Wang, W. Han, K. Zhao, L. Zhu, Y.
603 Hu, H. Xue, Y. Ma, L. Zhang, J. Nie, R. Zhou, S. Li, H. Liu, and Y. Zhu, 2019: Review of Chinese
604 atmospheric science research over the past 70 years: Synoptic meteorology. *Science China Earth Sciences*,
605 **62**, 1946-1991, doi:10.1007/s11430-019-9534-6.
- 606 Mlawer, E. J., S. J. Taubman, P. D. Brown, M. J. Iacono, and S. A. Clough, 1997: Radiative transfer for
607 inhomogeneous atmospheres: RRTM, a validated correlated-k model for the longwave. *Journal of*
608 *Geophysical Research: Atmospheres*, **102**, 16663-16682, doi:10.1029/97JD00237.
- 609 Pucik, T., P. Groenemeijer, I. Tsonevsky, 2021: Vertical wind shear and convective storms.
610 <https://www.ecmwf.int/en/elibrary/81211-vertical-wind-shear-and-convective-storms>
- 611 Rao, C., G. Chen, and L. Ran, 2023: Effects of Typhoon In-Fa (2021) and the Western Pacific Subtropical High



- 612 on an Extreme Heavy Rainfall Event in Central China. *Journal of Geophysical Research: Atmospheres*,
- 613 **128**, e2022JD037924, doi:<https://doi.org/10.1029/2022JD037924>.
- 614 Rotunno, R., J. Klemp, and M. Weisman, 1988: A Theory for Strong, Long-Lived Squall Lines. *Journal of The*
- 615 *Atmospheric Sciences - J ATMOS SCI*, **45**, 463-485, doi:10.1175/1520-
- 616 0469(1988)045<0463:ATFSL>2.0.CO;2.
- 617 Schumacher, R. S., and K. L. Rasmussen, 2020: The formation, character and changing nature of mesoscale
- 618 convective systems. *Nature Reviews Earth & Environment*, **1**, 300-314, doi:10.1038/s43017-020-0057-7.
- 619 Stauffer, D. R., N. L. Seaman, and F. S. Binkowski, 1991: Use of Four-Dimensional Data Assimilation in a
- 620 Limited-Area Mesoscale Model Part II: Effects of Data Assimilation within the Planetary Boundary Layer.
- 621 *Monthly Weather Review*, **119**, 734-754, doi:10.1175/1520-0493(1991)119<0734:UOFDDA>2.0.CO;2.
- 622 Sun, J., L. Qi, and S. Zhao, 2006: A study on mesoscale convective systems of the severe heavy rainfall in north
- 623 China by “9608” typhoon. *Acta Meteorologica Sinica*, **64**, 57-71, doi:10.11676/qxxb2006.006.
- 624 Sun, Y., Z. Zhong, L. Yi, T. Li, M. Chen, H. Wan, Y. Wang, and K. Zhong, 2015: Dependence of the relationship
- 625 between the tropical cyclone track and western Pacific subtropical high intensity on initial storm size: A
- 626 numerical investigation. *Journal of Geophysical Research: Atmospheres*, **120**, 11,451-411,467,
- 627 doi:<https://doi.org/10.1002/2015JD023716>.
- 628 Tewari, M., F. Chen, W. Wang, J. Dudhia, M. A. LeMone, K. Mitchell, M. Ek, G. Gayno, J. Wegiel, and R. H.
- 629 Cuenca, 2004: Implementation and verification of the unified NOAA land surface model in the WRF
- 630 model. 20th conference on weather analysis and forecasting/16th conference on numerical weather
- 631 prediction, pp. 11-15.
- 632 Thompson, G., P. R. Field, R. M. Rasmussen, and W. D. Hall, 2008: Explicit Forecasts of Winter Precipitation
- 633 Using an Improved Bulk Microphysics Scheme. Part II: Implementation of a New Snow Parameterization.
- 634 *Monthly Weather Review*, **136**, 5095-5115, doi:doi:10.1175/2008MWR2387.1.
- 635 Wang, Y., Y. Wang, and H. Fudeyasu, 2009: The Role of Typhoon Songda (2004) in Producing Distantly Located
- 636 Heavy Rainfall in Japan. *Monthly Weather Review*, **137**, 3699-3716,
- 637 doi:<https://doi.org/10.1175/2009MWR2933.1>.
- 638 Xia, R., and D.-L. Zhang, 2019: An Observational Analysis of Three Extreme Rainfall Episodes of 19–20 July
- 639 2016 along the Taihang Mountains in North China. *Monthly Weather Review*, **147**, 4199-4220,



- 640 doi:10.1175/MWR-D-18-0402.1.
- 641 Xu, H., and X. Li, 2017: Torrential rainfall processes associated with a landfall of Typhoon Fitow (2013): A
642 three-dimensional WRF modeling study. *Journal of Geophysical Research: Atmospheres*, **122**, 6004-6024,
643 doi:https://doi.org/10.1002/2016JD026395.
- 644 Xu, H., D. Zhang, and X. Li, 2021: The Impacts of Microphysics and Terminal Velocities of Graupel/Hail on the
645 Rainfall of Typhoon Fitow (2013) as Seen From the WRF Model Simulations With Several Microphysics
646 Schemes. *Journal of Geophysical Research: Atmospheres*, **126**, e2020JD033940,
647 doi:https://doi.org/10.1029/2020JD033940.
- 648 Xu, H., X. Li, J. Yin, and D. Zhang, 2023a: Predecessor Rain Events in the Yangtze River Delta Region
649 Associated with South China Sea and Northwest Pacific Ocean (SCS-WNPO) Tropical Cyclones. *Advances
650 in Atmospheric Sciences*, doi:10.1007/s00376-022-2069-3.
- 651 Xu, H., D. Zhao, J. Yin, Y. Duan, W. Gao, Y. Li, and L. Zhou, 2023b: Indirect Effects of Binary Typhoons on an
652 Extreme Rainfall Event in Henan Province, China From 19 to 21 July 2021. 3. Sensitivities to Microphysics
653 Schemes. *Journal of Geophysical Research: Atmospheres*, **128**, e2022JD037936,
654 doi:https://doi.org/10.1029/2022JD037936.
- 655 Yang, L., M. Liu, J. A. Smith, and F. Tian, 2017: Typhoon Nina and the August 1975 Flood over Central China.
656 *Journal of Hydrometeorology*, **18**, 451-472, doi:10.1175/JHM-D-16-0152.1.
- 657 Yin, J., D.-L. Zhang, Y. Luo, and R. Ma, 2020: On the Extreme Rainfall Event of 7 May 2017 Over the Coastal
658 City of Guangzhou. Part I: Impacts of Urbanization and Orography. *Monthly Weather Review*, **148**, 955-
659 979, doi:10.1175/MWR-D-19-0212.1.
- 660 Yin, J., X. Liang, H. Wang, and H. Xue, 2022a: Representation of the autoconversion from cloud to rain using a
661 weighted ensemble approach: a case study using WRF v4.1.3. *Geosci. Model Dev.*, **15**, 771-786,
662 doi:10.5194/gmd-15-771-2022.
- 663 Yin, J., D. Wang, Z. Liang, C. Liu, G. Zhai, and H. Wang, 2018: Numerical Study of the Role of Microphysical
664 Latent Heating and Surface Heat Fluxes in a Severe Precipitation Event in the Warm Sector over Southern
665 China. *Asia-Pacific Journal of Atmospheric Sciences*, **54**, 77-90, doi:10.1007/s13143-017-0061-0.
- 666 Yin, J., H. Gu, M. Yu, X. Bao, Y. Xie, and X. Liang, 2022b: Synergetic Roles of Dynamic and Cloud
667 Microphysical Processes in Extreme Short-Term Rainfall: A Case Study. *Quarterly Journal of the Royal*



- 668 *Meteorological Society*, **148**, 3660- 3676, doi:<https://doi.org/10.1002/qj.4380>.
- 669 Yin, J., H. Gu, X. Liang, M. Yu, J. Sun, Y. Xie, F. Li, and C. Wu, 2022c: A Possible Dynamic Mechanism for
- 670 Rapid Production of the Extreme Hourly Rainfall in Zhengzhou City on 20 July 2021. *Journal of*
- 671 *Meteorological Research*, **36**, 6-25, doi:10.1007/s13351-022-1166-7.
- 672